1. Introduction

Hydrothermal carbonization (HTC) is a process by which wet biomass can be directly converted to a solid carbonaceous material, called hydrochar. HTC is usually performed on biomasses with moisture > 50% at 150–250 °C in closed reactors, under autogenously generated pressure (Khan et al., 2021). These conditions induce hydrolysis (mainly polysaccharides to oligo-monosaccharides), intra- and intermolecular de-hydration and polymerization, and result in the synthesis of aromatic clusters with lower H/C and O/C as carbonized end-products (Jain et al., 2016; Khan et al., 2021). Hydrochar can be synthesized by reactions occurring directly on the solid biomass particles (primary char) or by polymerization of the soluble molecules (secondary char) (Jain et al., 2016). A minor fraction of C is converted to liquid and gaseous products (Erses Yay et al., 2021; Jain et al., 2016). The main parameters affecting the yield and properties of the produced hydrochar are reaction temperature, residence time, solid/liquid ratio, the chemical composition of the biomass, and the liquid phase used (Jain et al., 2016; Khan et al., 2021). Hydrochar has been tested for several applications, including the production of catalytic supports (Jain et al., 2016), fuels, soil amendment, and adsorbents for heavy metal removal (Fang et al., 2018). So far, less attention has been given to producing adsorbents for the removal of anions, like arsenates. Arsenic (As) is a toxic and carcinogenic element (Group I) (IARC, 2012), and its ingestion can cause several health issues, such as vascular diseases and skin alterations (IARC, 2012; Ungureanu et al., 2015). As ranks 1st in the U.S.A. National Priorities List (NPL) of the Agency for Toxic Substances and Disease Registry (ATSDR, 2019). Unfortunately, conventional adsorbents used to remove As from contaminated water (such as granular ferric oxides/hydroxides) are expensive (5-10 €/kg). Their high cost is one of the main limits in providing safe drinking water in polluted areas (Driehaus, 2002). For this reason, the production of low-cost adsorbents from cheap resources, such as agro-industrial byproducts and wastes, is worthy of investigation. Uncarbonized biomass was already reported as an adsorbent for As removal in previous studies (Zoroufchi Benis et al., 2020). However, a significant limitation of

such adsorbent is its instability in real water treatment plants, mainly due to microbial degradation (Peydayesh and Mezzenga, 2021). Carbonization is important to fix C and to give long-term stability to the adsorbent. Biochar from dry pyrolysis has been largely studied to produce of adsorbents for As, which are obtained by functionalization with Fe oxides in water solution containing Fe salts (Li et al., 2018). However, adding and removing water to a dry material (for Fe functionalization) requires energetically expensive unit operations. HTC can be more efficiently integrated with Fe functionalization because wet biomass material is directly carbonized in the water phase during HTC.

In a previous study, a process was proposed to couple HTC with Fe oxides/hydroxides functionalization, to obtain an adsorbent for As removal (Capobianco et al., 2020). The control of pH in the reactor was found fundamental for the performance of the process, because initial alkaline pH (pH_i) induces both low adsorbent yields and instability in the water of the produced adsorbent, although higher Fe content and As adsorption are obtained. Acid pH's give better stability but lower Fe content and As adsorption capacity. A two-stage process was proposed, in which Fe was initially added in the first HTC treatment at acid pH and eventually precipitated with high yield at alkaline pH to obtain an adsorbent with both water stability and good As adsorption capacity. The effect on HTC of varying the pH_i was not elucidated in previous studies, and a first unanswered issue is why pH changes during HTC. In previous studies where the pH_i was varied, it turned out that the final pH value was the same at the end of the process (Flora et al., 2013; Reza et al., 2015; Wang et al., 2017), irrespective of the pH_i in the HTC process. The main reasons for such pH variations are the buffer property of the biomass and the reaction products, and the difficulty of performing an online pH control in HTC reactors. Recently, a relevant difference in the final pH was evidenced by initially setting three largely different pH_i values (0.9, 7, and 14) (Capobianco et al., 2020). The study found relevant effects on the hydrochar yield, but the kinetic behavior was not reported. The effects on HTC kinetics of a pH variation and its influence on the products remain largely unexplored.

The present study aim at first understanding how the choice of pH_i affects the kinetics of hydrochar production and how pH changes during HTC, and secondly, at optimizing the operative conditions used to functionalize hydrochar with Fe.

Different HTC treatments were singularly performed and stopped at different reaction times to achieve the first goal. In addition, three different acid pH_i values were tested, based on a previous study, showing that alkaline pH's bring to relevant lignin hydrolysis (Capobianco et al., 2020).

To achieve the second goal, previous studies, performed within a single set of parameters for Fe precipitation, were expanded (Capobianco et al., 2020; Chen et al., 2021; Khan et al., 2019; Zhu et al., 2014). An industrial scale-up of such process may require exploring and optimizing parameters such as the Fe/hydrochar ratio and the hydrochar and Fe single concentrations, because they can affect the As adsorption capacity of the obtained adsorbent, and the economic and environmental sustainability of its production process.

2. Materials and methods

2.1 Materials

Olive pomace (OP) was collected from a continuous three-phase olive oil mill plant at Rocca Massima (LT, Italy) managed by Coop. Agricola Sant'Antonio. OP was dried at 60 °C until constant weight, manually ground in an agate mortar and finally sieved to remove particles > 1 mm, mainly composed of olive stones and leaves (Fig. S1). The fraction < 1 mm was 45% of the initial OP mass. H_2SO_4 (95%), HNO_3 (65%), H_2O_2 (30%), $FeCl_2 \cdot 4H_2O$ (97%), $FeCl_3 \cdot 6H_2O$ (99%), NH_4OH (25% solution) and KH_2AsO_4 (98-102%, A6631) were purchased from Merck/Sigma Aldrich.

2.2 Hydrothermal carbonization (HTC)

Hydrochar was synthesized by mixing 5.0 g of OP with 20 mL feedwater solution (25% w/v) in 100 mL polytetrafluoroethylene (PTFE) vessel. HTC was performed at different pH_i and reaction times using the Milestone Laboratory Microwave System Labstation. Three different feedwater solutions were tested: distilled water (pHi = 5.6); H_2SO_4 67.5 mM (pH_i = 2.0); H_2SO_4 0.45 M

(pH_i = 0.5). Each pHi was measured after biomass homogenization. The following heating program was operated: 5 min preheating up to 200 °C, 5 – 120 min reaction time (t) at 200 °C, 60 min cooling in a water bath at room temperature. After cooling, the vessels were opened and left for 30 min under the fume hood. For each different reaction time and each pH_i, HTC was repeated twice inside independent vessels. The solid product obtained (hydrochar) was recovered by vacuum filtration through 8-12 μm filter paper (VWR International, cat. N^o 516-0264), then washed with 70 mL distilled water through the filter and finally dried at 105 °C (m_{HC}). Permeates were stored at - 20 °C before pH analysis. Hydrochar mass yield (% w/w) was calculated by Eq. 1:

$$Y_{HC}\ (\%) = \frac{m_{HC}}{m_{OP}}\ 100 \quad (1)$$

where m_{OP} is the initial olive pomace mass.

C mass yield was calculated by Eq. 2:

$$Y_{C/C} = \frac{m_{HC} f_{C/HC}}{m_{OP} f_{C/OP}}\ 100 \quad (2)$$

where $f_{C/HC}$ and $f_{C/OP}$ are the C fractions inside hydrochar and initial olive pomace, respectively.

N mass loss was calculated by Eq. 3:

$$N\ mass\ loss = \frac{(m_{OP} f_{N/OP}) - (m_{HC} f_{N/HC})}{m_{OP} f_{N/OP}} \quad (3)$$

where $f_{N/HC}$ and $f_{N/OP}$ are the N fractions inside hydrochar and olive pomace, respectively.

2.3 Iron precipitation

The composite material hydrochar/iron oxide was synthesized using four conditions through a 2^2 factorial experimental design, varying hydrochar and Fe concentration (Table 1). Hydrochar obtained at pH_i = 0.5 after 30 min HTC reaction was employed. The protocol for precipitation was taken from Khan et al. (2019), with modifications on hydrochar and Fe concentration. A 100 mL glass reactor was filled with 50 mL distilled water, and a defined amount of hydrochar powder was added (Table 1). The reactor was equipped with a water jacket for temperature control, kept under constant N_2 flow and magnetic stirring, and equipped with a condensation column. After 10

min at room temperature, $FeCl_2 \cdot 4H_2O$ and $FeCl_3 \cdot 6H_2O$ were added (Table 1) and mixed for 30 min. The temperature was then increased to 80 °C for 30 min with a thermostatic bath (Lauda EcosSilver Re 620); after that, 200 mL/L NH_4OH 25% were added drop wise. Finally, the solid phase was subsequently recovered through 5 min centrifugation at 4500 rpm. The solid phase obtained was washed five times with 40 mL distilled water, filtered through 8-12 μm filter paper, and dried at 105 °C.

Sample name	$[Fe^{3+}]$ (mmol/L)	$[Fe^{2+}]$ (mmol/L)	Hydrochar (g/L)	Fe/hydrochar
5L	44	30	5.0	0.82
5H	81	55	5.0	1.52
200L	44	30	200	0.021
200H	81	55	200	0.038

Table 1. Experimental conditions tested for the optimization of the iron oxides co-precipitation conditions. Reaction volume: 50 mL.

Fe precipitation yield ($Y_{Fe/Fe}$) was calculated by Eq. 4:

$$Y_{Fe/Fe} = \frac{m_{HC} f_{Fe/HC}}{m_{Fe}} 100 \quad (4)$$

where m_{HC} is the mass of hydrochar recovered after Fe precipitation, $f_{Fe/HC}$ is the Fe fraction inside the recovered hydrochar and m_{Fe} is the whole Fe mass added in the reactor.

2.4 Arsenic adsorption tests

As adsorption tests were carried out for the samples 5H and 200H obtained (Table 1). Samples were ground on an agate mortar until obtaining a granulometry < 1000 μm, then 50 mg were added inside a 50 mL polypropylene tube with 25 mL solution 15 mg/L As. The suspension was stirred at 700 rpm by a polyethylene mechanical impeller for 1200 min, which should allow for attaining equilibrium, as previously reported (Capobianco et al., 2020). The pH was set throughout the test at 5.0 ± 0.2 by adjusting it with 0.05 M NaOH or 0.05 M HCl. Finally, the suspension was

centrifuged at 5000 rpm for 10 min and the supernatant was stored at - 20 °C before As analysis. The adsorption capacity (q) was calculated by Eq. 5:

$$q\ \left(\frac{mg}{g}\right) = \frac{(C_0 - C_f)V}{m_{HC}} \quad (5)$$

where C_0 and C_f are the As concentrations before and after the adsorption test, respectively, V is the volume, and m_{HC} is the mass of the adsorbent.

The effect of changing the stirring procedure was tested by comparing the hydrochar produced with a two-stage protocol (Capobianco et al., 2020) etither as already described above (stirring with impeller), or by adding 100 mg hydrochar inside a 150 mL glass flask filled with 50 mL As solution 15 mg/L, applying magnetic stirring at 700 rpm for 1200 min.

2.5 Chemical analyses

For acid digestion, 100 mg of hydrochar were mixed with 8 mL HNO_3 65% and 2 mL H_2O_2 30% in a 100 mL PTFE vessel, then heated by microwave by following the digestion program: 2 min from 25 °C to 85 °C, 5 min from 85 °C to 145 °C, 3 min from 145 °C to 200 °C, 20 min at 200 °C and 30 min for cooling. At the end, samples were filtered through 0.7 μm glass fiber filters and analyzed for Fe content by Atomic Adsorption Spectroscopy (AAS) with contrAA® 300 Analytik Jena AG. The pH was measured with a glass electrode (InLab® Expert Pro ISM®, Mettler Toledo) calibrated with standard solutions at pH 4.0, 7.0 and 9.0. Ash content was measured by treating 100 mg sample in a crucible at 600 °C for 22 h and calculated by Eq. 6:

$$Ash\ (\%) = \frac{m_{ash}}{m_{HC}} 100 \quad (6)$$

where m_{ash} is the weight of ashes measured after treatment at 600 °C.

Elemental composition was determined by CHNS analysis carried out by an elemental analyzer (EA 1110 CHNS/O). As concentration was determined by an inductively coupled plasma optical emission spectrometry (ICP-OES; Vista MPX CCD Simultaneous, Varian, Victoria, Mulgrave, Australia) in axial view mode and equipped with a cyclonic glass chamber. The ICP-OES

operating parameters were reported elsewhere (Astolfi et al., 2017). Calibration standards of As were prepared daily by diluting a single standard solution at 1000 ± 2 mg/L (Merck, Darmstadt, Germany) in 2% (v/v) HNO_3. Yttrium (Y) at 0.2 mg/L (from 1000 ± 2 mg/L; Panreac Química, Barcelona, Spain) was used as an internal standard for ICP-OES measurements. The following wavelengths (nm) were used: As 188.980 and Y 371.029. Scanning electron microscope (SEM) analysis was performed with HR-FESEM (High Resolution Field Emission SEM), model AURIGA Zeiss, which includes the EDX (Energy Dispersive X-ray Spectroscopy) microanalysis. Before analysis, few milligrams of samples were ground, sieved through a 1000 μm sieve, and sizzled with a thin chromium layer.

The elemental electronic state and surface atomic composition of samples were analyzed by X-ray Photoelectron Spectroscopy (XPS, Omicron NanoTechnology modified MXPS system). The spectra were excited by Mg Kα photons (hν = 1253.6 eV), operating the anode at 14 kV and 14 mA. All the photoionization regions were acquired using an analyzer pass energy of 20 eV, and take-off angles of 53° to the sample surface normal were adopted. The experimental spectra were theoretically reconstructed by fitting the secondary electrons background to a Shirley function and the elastic peaks to pseudo-Voigt functions described by a common set of parameters (position, FWHM, Gaussian-Lorentzian ratio) free to vary within narrow limits. The 5H and 200H samples were measured as compact tablets obtained by a 13 mm diameter mold operated at the pressure of 10 ton.

2.6 Statistical treatment of data

All experiments were conducted in duplicate, in which each replicate corresponded to a hydrochar obtained from an independent synthesis process. Error bars were calculated as standard deviation (SD). The MATLAB function ‘nlinfit’ was used for nonlinear fitting by minimizing the sum of the squared residuals. Differences between sample means were determined using t-test and one-way analysis of variance (ANOVA). ANOVA was applied only to assess the effect of N mass

loss; in this case, data collected at 30 min and 60 min were considered as replicate, and n was 4. The significance of linear correlations was verified by determining the significance of the angular coefficient. Statistical tests were performed on Microsoft Excel. A significance level of 5% (α = 0.05) was considered for all tests.

3. Results and discussion

3.1 Effect of initial pH and reaction time on hydrothermal carbonization

Hydrothermal carbonization was performed by comparing three different pH_i: 5.6 (the autogenous pH obtained by using distilled water as feedwater), 2.0, and 0.5 (these latter obtained by adding H_2SO_4). H_2SO_4 was preferred to other acids because SO_4^{2-} is less problematic than other anions (e.g., Cl^- and NO_3^-) for reactor corrosion. A pH variation during the process was expected at different reaction times mainly from the production of organic acids by degradation of sugars and biomolecule leaching (Hoekman et al., 2011). When the biomass was put in contact with pure water, the pH_i was 5.6 due to the buffer property of the biomass functional groups. During the HTC, the pH dropped down from 5.6 to 3.5 in the first 30 min. After that, it raised again to a stable value of 4.1 (± 0.1) (Fig. 1a). The pH drop found in the initial phase agrees with what is expected from previous studies (Hoekman et al., 2011). Its origin was the degradation of sugars and other biomolecules to form organic acids (Hoekman et al., 2011). In addition to this, Fig. 1 also shows a pH increase in the latter phase between 30 min and 60 min. Such increase was likely due to the polymerization of soluble organic acids producing secondary char (Jain et al., 2016). For pH_i 2.0 and 0.5, the pH respectively initially increased from 2.00 to 2.60 (± 0.01) in 30 min, and from 0.50 to 0.96 (± 0.04) in 15 min (Fig. 1c). Even in this case, the initial pH variation is likely due to the produced organic acids. The usual range of pKa values for carboxylic groups from peptides and hemicellulose is between 2.5 and 5.0 (Di Caprio et al., 2014). This explains why, starting from pH > 5, the pH of the resulting solution decreased, while it increased from pH < 2.5. The pH trend changed again for longer reaction times for pH_i 2.0 and 0.5. The pH decreased after 30 min from 0.96 (± 0.04) to 0.72 (± 0.02) for pH_i 0.5 and from 2.60 (± 0.01) to 1.85 (± 0.10)

after 20 min for pH_i 2.0 (Fig. 1c). Similar to what was discussed for pH 5.6, and pH_i 0.5 and 2.0, the inverted trend for longer reaction times was likely due to the polymerization of soluble compounds to form secondary char. Hydrochar yield (Y_{HC}) varied with time following a first-order model for pH_i 5.6 (Fig. 1b), with a kinetic constant (k) = 0.185 min^{-1} (± 0.07 min^{-1}) (τ = 5.4 min). For pH_i 0.5, a first-order model was inadequate, because Y_{HC} varied following a not-monotonic behavior (Fig. 1d). In this case, the Y_{HC} dropped to 45.4% (± 0.9%) in 5 min and gradually increased to a final value of 52.9% (± 0.9%) at 60 min. This behavior agrees with the mechanism described for pH variation. It is consistent with prevailing hydrolysis and leaching in the initial phase (reduced Y_{HC}), followed by the polymerization of the soluble compounds at a longer time, resulting in increased Y_{HC}. It is possible that either of the two mechanisms was involved for pH_i 5.6, but in this case, the impact of the initial hydrolysis was negligible. The rapid drop in mass yield registered for pH 0.5 could suggest that temperature has a scarce influence on the hydrolysis reactions for such a low pH. To confirm the important role of the temperature for pH_i = 0.5, this condition was also tested at 30 and 60 min reaction time at 25 °C (Fig. S2). At 25 °C, the mass yield was 83.8% (± 0.5%), much higher than 200 °C, confirming that the temperature is fundamental for a relevant hydrolysis/de-hydration of olive pomace.

Carbonization yield can be better assessed by looking at the increment of C% inside the hydrochar during HTC (Fig. 2a). For pH_i 0.5, the C% remarkably increasedalready from 51.6% (± 0.7%) to 67.2% (± 0.4%) after 10 min and to 71% (± 2%) after 30 min. This suggests that in the initial phase (< 30 min), hydrolysis and solubilization of biomolecules proceeds along with a remarkable de-hydration.

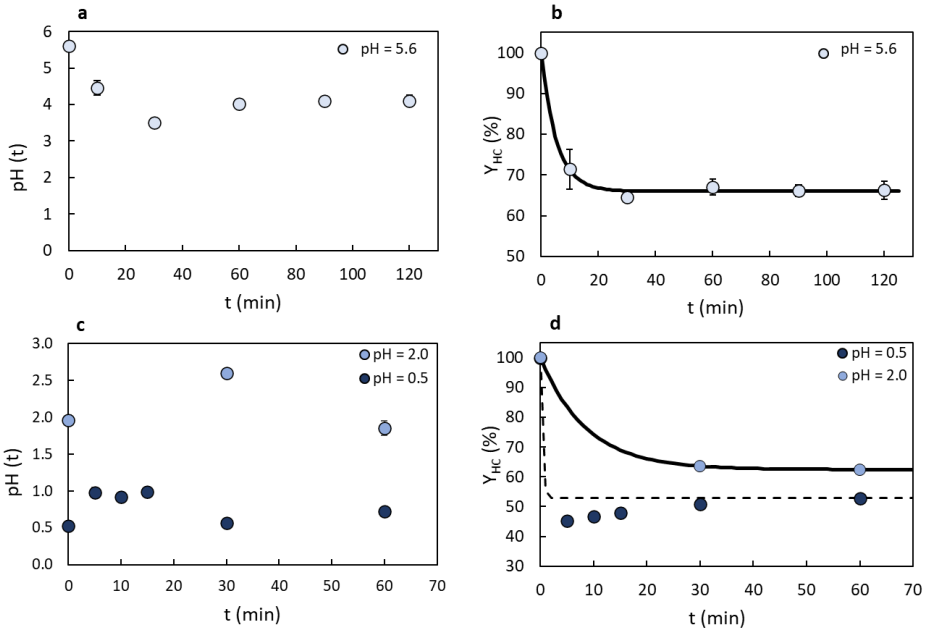

Figure 1. Value of pH (*a*-*c*) and hydrochar yield Y_{HC} (*b*-*d*) at different reaction times and for different pH_i of 0.5, 2.0 (*c*-*d*) and 5.6 (*a*-*b*). Results of fitting with first order model are indicated with lines. Results are reported as mean ± SD (n = 2).

For the three pH_i, no relevant increase in C% was detected after 30 min, with a final C% of 72% (± 1%), 63% (± 2%), and 58% (± 2%) for pH_i 0.5, 2.0 and 5.6 respectively. This result confirms the remarkable positive effect given by the acid pH on the carbonization yield. The pH_i 0.5 allowed to attain 72% C, higher than those obtained in a previous study (65.1%) for the same kind of biomass, but at 250 °C (Volpe and Fiori, 2017), indicating how acid can be exploited to avoid higher process temperature. The analysis of the evolution of C mass yield, $Y_{C/C}$ (Fig. 2b), confirmed the above assignment of pH variations to initial hydrolysis followed by polymerization. For pH_i 0.5, the C mass yield was only 62% (± 2%) after 10 min, and then increased up to 74% (± 3%) after 60 min, indicating polymerization of soluble organic carbon, forming secondary char. Such behavior was not found for pH_i 2.0 and 5.6 in the investigated range of time. Initial hydrolysis was more remarkable for pH_i 0.5, because a low pH can catalyze the hydrolysis of polysaccharides to simple sugars (Moxley and Zhang, 2007). In turn, a higher concentration of hydrolysis products can enhance the subseqeunt synthesis of secondary char. The pH_i affected O/C and H/C obtained in the hydrochar at different reaction times.

For the three pH_i, H/C and O/C mainly decreased in the first 30 min of reaction. The carbonization efficiency increased at lower pH, as evidenced by the Van Krevelen diagram (Fig. 2c-e). The effect of acid pH was more remarkable on O/C than on H/C (Fig. 1c), likely because higher H^+ concentration also increased the protonation of the hydrochar oxygenate groups. However, it cannot be excluded that lower pH favored de-carboxylation over de-hydration too. To verify the protonation effect, the hydrochar obtained by HTC at pH_i 0.5 was rinsed seven times with water. As a result, H/C decreased ($p = 0.026$, $n = 2$) from 1.31 (± 0.04) to 1.16 (± 0.02), confirming the relevant effect of hydrochar protonation. N content in the hydrochar did not vary throughout HTC when the pH_i was 5.6 and 2.0, while it remarkably decreased for pH_i 0.5 from 1.7% (± 0.1%) to 0.99% (± 0.04%) after 10 min and remained stable afterward (Fig. 1f). This behavior was due to the acid-catalyzed hydrolysis of protein's peptide bound (Fountoulakis and Lahm, 1998), resulting in the release of N in the form of amino acids and peptides. The released ammonium groups could increase the pH observed in the initial phase (Fig. 1c).

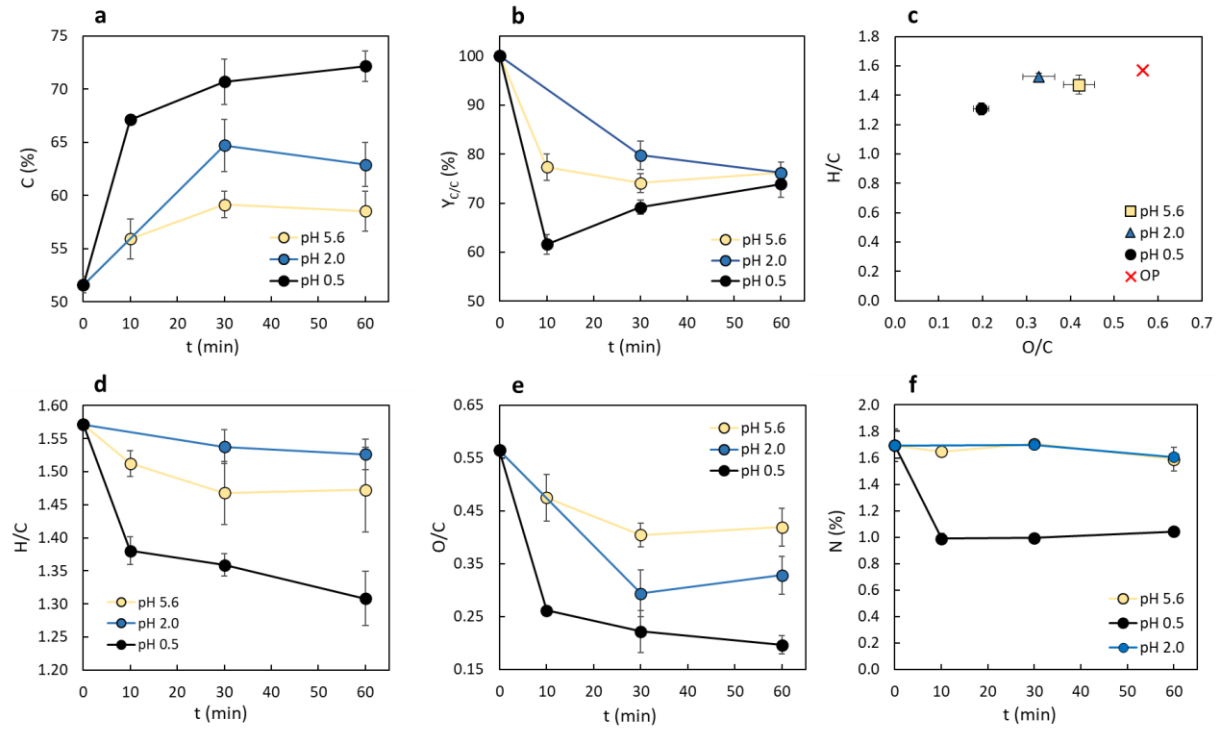

Figure 2. Kinetics of carbonization progression for different values of pH_i. *a*) Variation of C% in the hydrochar. *b*) Mass yield for C from biomass to hydrochar. *c*) Van Krevelen diagram of the hydrochars

obtained at different pH_i after 30 min. *d*) Variation of H/C molar ratio in the hydrochar. *e*) Variation of O/C molar ratio in the hydrochar. *f*) Variation of N content in the hydrochar. Results are reported as mean ± SD (n = 2).

A mass balance for N confirmed a relevant loss of N from the solid phase during its conversion from biomass to hydrochar (Fig. 3a). Such N loss was two times higher for pH_i 0.5 than for pH_i 5.6 and 2.0 ($p = 3 \cdot 10^{-8}$, n = 4). For pH_i 5.6 and 2.0, N loss was higher than those reported in a previous study (20-30%) (Capobianco et al., 2020), despite the same biomass and comparable pH being used. The higher temperature used in this study (200 °C instead of 170 °C) was likely the reason. No relevant difference was observed by comparing the results at 30 min and 60 min.

The final pH measured after 60 min was lower than the pH_i, and it was linearly related to its initial value ($p = 9 \cdot 10^{-6}$). Therefore, the attained final pH can be predicted by the equation reported in Fig. 3b. This finding apparently contradict with previous studies in which no relevant relation was found between the feedwater pH (2-12) and the final pH (Flora et al., 2013; Reza et al., 2015). Thus, the key difference in this study was to consider as pH_i the one attained after an initial phase of biomass mixing with the feedwater (before starting HTC), in place of the sole feedwater pH. In this way we could overcome the effect of the buffer activity of the biomass, that hindered an effective pH control in previous studies.

In Fig. 3c-e the relation of the pH attained in the reaction solution at arbitrary reaction times (t), with the different factors indicative for the performance of the HTC process, is shown.

The hydrochar mass yield, Y_{HC}, usually inversely proportional to the carbonization yield, was found only loosely related to the pH in the water phase (measured at different reaction times) in the range 1.8 – 4.3. Such relation was much more evident at pH's below 1.8 (Fig. 3c), indicating that only in these conditions the hydrolysis and de-hydration reactions are remarkably affected. C% and O/C ratio were both linearly correlated ($p = 2 \cdot 10^{-16}$ and $5 \cdot 10^{-3}$ respectively) with the pH measured at different reactions times during HTC (Fig. 3d-e), indicating that the actual pH value

can be used as a predictive parameter for such values. Measuring the pH instead of the C content is easier, and this finding suggests a cheap control system for the HTC process. Notice that the H/C ratio (Fig. 3f) was not statistically related to the pH ($p = 0.09$), because of the protonation occurring on the hydrochar.

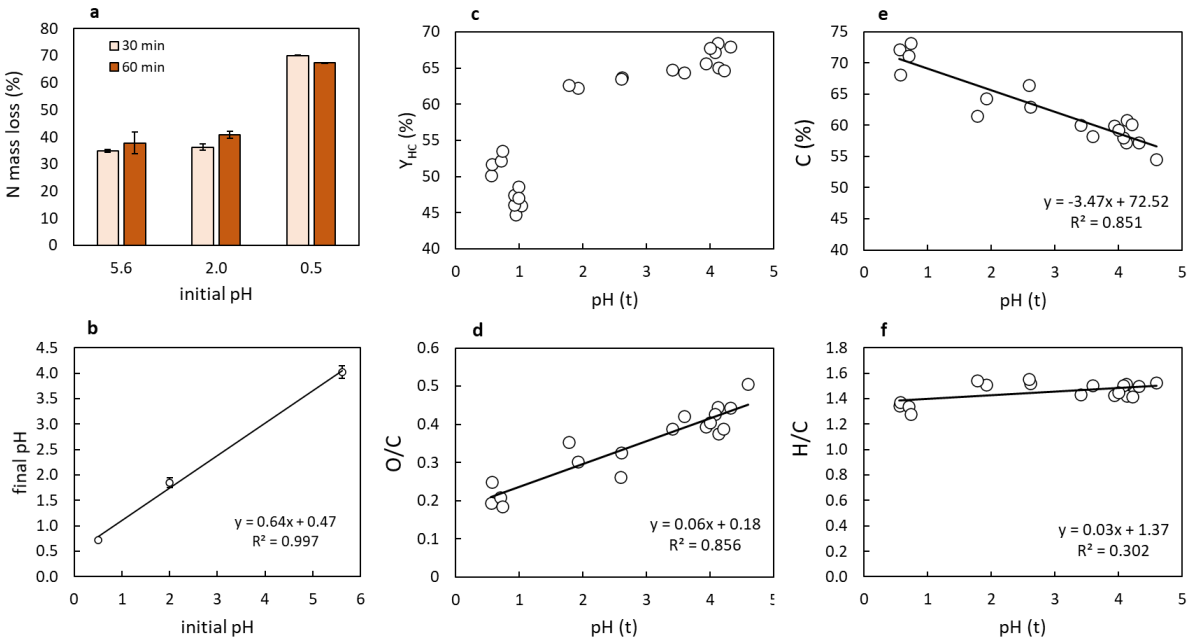

Figure 3. Loss of N mass from the solid phase at the end of HTC performed at different treatment times and initial pH (*a*). Correlation between initial and final pH after 60 min HTC (*b*). Data are reported as mean ± SD (n = 2). Correlation between pH measured during HTC (at different reaction times) and biomass to hydrochar mass yield Y_{HC} (*c*), O/C in the hydrochar (*d*), C % in the hydrochar (*e*) and H/C in the hydrochar (*f*).

3.2 Effect of Fe and hydrochar concentrations on Fe precipitation

A previous study indicated that hydrochar functionalization with iron oxides is a key factor in increasing As adsorption capacity (Capobianco et al., 2020). However, little work was done towards optimizing the conditions for Fe precipitation. To develop an industrial process, hydrochar concentration should be maintained as high as possible to minimize reactor volume, water consumption and costs. However, high hydrochar concentration can affect Fe precipitation

yield ($Y_{Fe/Fe}$) and the quality of the obtained product. Therefore, different co-precipitation conditions were tested in this study, to evaluate the qualitative and quantitative effects of hydrochar and Fe concentration on the produced composite material. As evidenced in Fig. 4a, $Y_{Fe/Fe}$ was affected by the hydrochar concentration ($p = 0.003$, $n = 4$). $Y_{Fe/Fe}$ was 66% (± 11%) and 100% (± 11%) for 200 g/L and 5 g/L hydrochar, respectively. This difference could be an effect of the higher concentration of organic compounds released at higher hydrochar concentration. These compounds could chelate Fe^{2+}/Fe^{3+} ions, increasing their solubility. The pH attained at the end of precipitation was 9.5 (± 0.4) and 10.2 (± 0.2), respectively, for the tests with 200 g/L and 5 g/L hydrochar. The lower pH for the test with higher hydrochar concentration was likely due to the hydrochar buffer property. However, it is not expected that such a small pH difference can affect $Y_{Fe/Fe}$ because, in the tested conditions, Fe_3O_4 should precipitate quantitatively in pH range 8 - 14 (Laurent et al., 2008).

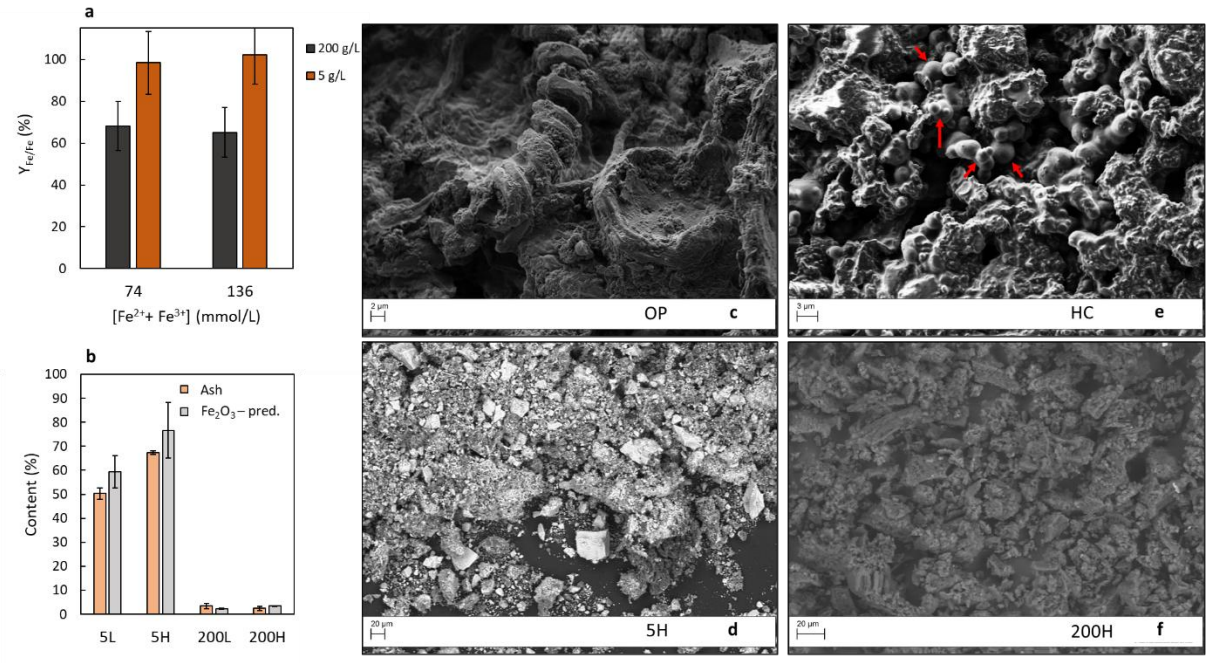

Figure 4. Fe precipitation yield ($Y_{Fe/Fe}$) from the liquid phase to the hydrochar for different hydrochar and Fe concentrations (*a*). Ash content measured in the different samples obtained after Fe precipitation as compared to the amount predicted by assuming complete conversion of Fe to Fe_2O_3 (*b*). The results are reported as mean ± SD (n = 2). SEM analysis of olive pomace (*c*), hydrochar obtained after 30 min HTC

at pH_i 0.5 (*e*), hydrochar obtained after Fe precipitation at hydrochar concentration 5 g/L (*d*) and 200 g/L (*f*). The arrows indicate secondary char deposits.

The different hydrochar concentrations (Table 1) determined the Fe fractions in the hydrochar recovered after precipitation (Table 2) due to the different Fe/hydrochar ratios (g/g) in the reactor. Such ratio was about 40 folds higher in the case of 5 g/L hydrochar (Table 1). In the 5L and 5H tests, Fe became the main element inside the hydrochar, amounting to 42% and 54%, respectively (Table 2). By assuming that the whole Fe present was in the form of Fe_3O_4, the content of Fe_3O_4 was 58% and 74% for 5L and 5H respectively. If the Fe_3O_4 percentage is summed to the C, H, N, and S ones, the mass balance close to 97% (± 8%) and 96% (± 10%) for 5L and 5H, respectively, indicating that the remaining fraction (Other%, in Table 2) was mainly composed by O in the form of Fe_3O_4. Higher Fe contents corresponded to higher ash contents (Fig. 4b). For all samples, ashes were consistent with a complete conversion of Fe to Fe_2O_3, as expected for the oxidative conditions used for ash analysis. In the conditions set for 200L and 200H, the Fe % obtained in the hydrochar after precipitation was only 1.6% or 2.41%, respectively, because of the lower Fe/hydrochar ratio and $Y_{Fe/Fe}$ (Fig. 4a). C and H in the hydrochar obtained after Fe precipitation came only from the initial hydrochar, therefore their content was lower after Fe precipitation, and inversely proportional to the Fe_3O_4% (Table 2).

	C %	H %	N %	S %	Fe %	Other %*
5L	35 ± 1	3.5 ± 0.3	0.80 ± 0.02	0.1 ± 0.1	42 ± 5	19 ± 7
5H	19.2 ± 0.1	2.0 ± 0.2	0.5 ± 0.1	-	54 ± 8	25 ± 8
200L	63.3 ± 0.1	6.6 ± 0.1	1.54 ± 0.06	0.054 ± 0.04	1.6 ± 0.2	26.9 ± 0.4
200H	62.3 ± 0.5	6.3 ± 0.7	1.36 ± 0.03	0.2 ± 0.2	2.41 ± 0.02	27 ± 1

Table 2. Elemental composition of the hydrochar obtained after Fe precipitation. C, H, N and S percentages were determined by CHNS, while Fe% by AAS. The results are reported as mean ± SD (n =

2). *The “Other%” component (mainly due to O) was calculated as 100 – (C% + H% + N% + S% + Fe %).

As shown in Table 2, N content in 5L and 5H was about half that in 200L and 200H. In samples 200H and 200L, N was about 50% higher than in the initial hydrochar (Fig. 2), indicating that N was derived from the initial hydrochar and from NH_4OH added for Fe precipitation. All samples showed a magnetic behavior, higher for the 5L and 5H samples, richer in Fe.

3.3 Sample characterization by XPS, SEM, and EDX

A detailed characterization of the obtained hydrochars was carried out fusing SEM, EDX, and XPS. The morphological analysis performed by SEM showed a remarkable difference between olive pomace and hydrochar obtained after 30 min HTC with pH_i 0.5 (Fig. 4c-e). Olive pomace showed a fibrous morphology derived from the vegetable fibers from olive fruits. In contrast after HTC the hydrochar showed amorphous structures and secondary char in the form of spherical granules with 2-3 μm diameter (Fig. 4e). It can be assumed that spherical particles are secondary char for three main reasons: i) They were absent before HTC; ii) Their morphology is closely consistent with the one reported for secondary char in previous studies (Jain et al., 2016; Volpe and Fiori, 2017); iii) The kinetic behavior of pH, mass yield and $Y_{C/C}$ (Fig. 1-2) indicates that C originated from soluble compounds formed solid particles. The hydrolysis of polysaccharides likely induced the loss of the fibrous morphology at the beginning of HTC. Hydrochars obtained after Fe precipitation showed different morphologies, depending on the different hydrochar concentrations used. In the test performed at 5 g/L, the obtained hydrochar showed a remarkable presence of crystals (square-shaped morphology) with sizes variable from < 1 μm to > 20 μm (Fig. 4d). They were absent before Fe precipitation, and likely formed by Fe precipitates. EDX confirmed this point, by showing a high content of Fe and O inside these structures, together with the absence of C species (Fig. S3). SEM (Fig. 4d) shows these crystals are mostly unlinked to the surrounding hydrochar. They were recovered together with the hydrochar powder mainly because they are insoluble. In addition, EDX showed Fe widely distributed on a large part of the hydrochar

surface in the form of structures with smaller sizes (Fig. S3). Large crystals were not detected in the samples obtained at 200 g/L (Fig. 4f), while EDX showed only Fe widely spread on the surface (Fig. S3). For low Fe/hydrochar ratio, the hydrochar surface was large enough to entrap Fe mainly in the form of small crystals precipitated on its pores. At a high Fe/hydrochar ratio, Fe also precipitated in larger crystal structures, which look independent from the hydrochar surface, likely because its pores might be saturated.

EDX also showed a relevant presence of the inorganic elements P, Mg, and K (Table 3) in the olive pomace, which disappeared after HTC, due to their leaching in water. The enrichment of the water phase in these mineral salts and the presence of N confirms a promising utilization of the residual water as fertilizer (Azzaz et al., 2020). The amount of C, O, N, and Fe determined by EDX followed the same trend obtained with CHNS and AAS (Table 2). However, some differences were found in the values because EDX analyzed mainly the surface layer. The elementary percentage amount EDX did not include H. S increased after HTC, because it was added as SO_4^{2-} as H_2SO_4. About 0.7% F was found in the hydrochar, likely deriving from the reactor in Teflon used for the HTC. Some Cu (0.4 – 1.5%) was also found on the olive pomace and hydrochar obtained after Fe precipitation; however, its specific origin is unclear. It could be a residue deriving from the Cu-based pesticides widely used as fungicides in olive farming (Glibota et al., 2019).

	C %	O%	N%	P%	Mg%	S%	K%	Cl%	Fe%	Cu%	F%	Al%
OP	55 ± 3	36 ± 4	4.8 ± 0.6	0.19 ± 0.01	0.10 ± 0.01	0.13 ± 0.00	2.5 ± 0.1	0.06 ± 0.00	0.02 ± 0.00	0.43 ± 0.09	-	-
HC	69.6 ± 0.1	25.4 ± 0.1	3.8 ± 0.4	-	-	0.37 ± 0.01	0.04 ± 0.04	0.04 ± 0.04	-	-	0.7 ± 0.3	-
5H	25.0 ± 0.2	27 ± 1	-	-	-	-	-	-	47 ± 1	1.3 ± 0.2	-	0.07 ± 0.07
200H	75 ± 5	15 ± 2	1.8 ± 0.2	-	-	0.20 ± 0.00	-	-	6.5 ± 0.2	1.5 ± 0.3	-	0.04 ± 0.04

Table 3. Elemental composition obtained by EDX for the olive pomace (OP), hydrochar obtained with pH_i = 0.5 (HC), and for the hydrochar samples obtained after Fe precipitation. Results were reported as mean ± SD (n = 2).

The results from XPS conducted on the sample 5H (after Fe precipitation) are reported in Fig. 5. The findings are almost identical to those from 200H, which are reported in Fig. S4. Fe was found in the form of Fe_3O_4, as verified by the presence in the Fe $2p_{3/2}$ region of three peaks at 710.7 eV, 712.5 eV and 715.6 eV, the first referring to Fe(II) and the second ones to Fe(III) components (Briggs and Seah, 1994). Therefore, it can be inferred that the crystal structures that appeared after Fe precipitation (Fig. 4d) were present as Fe_3O_4.

The O 1s signal was composed of three peaks, falling at ~530 eV, ~532 eV, and ~534 eV, respectively, corresponding to metal oxides, organic oxygenated compounds, and chemisorbed water. The C 1s region was theoretically reconstructed by three peaks, falling at 285 eV, 286 eV, and 288 eV. These components respectively correspond to C-C, C-X (X = O, halogens), and carbonyl/carboxylic groups and indicate the presence of a relevant amount of oxygenated carbon groups. A less intense peak at 291 eV corresponds to aromatic groups (π to π^* peak transition). The N 1s region showed a peak at 407.6 eV, assigned to nitrate, and a second at 400.7 eV, likely corresponding to amine groups. In the sample 200H, the nitrate signal was higher than in 5H, suggesting that this group derived from the hydrochar. XPS analysis also showed other minor elements, such as S (present as sulphate), Ca, Si, Cl, and Cu (II), confirming the results previously obtained with EDX. The further presence of Cr, not found with EDX, could be traced to minor contamination introduced by the preparation of the tablet for XPS measurements.

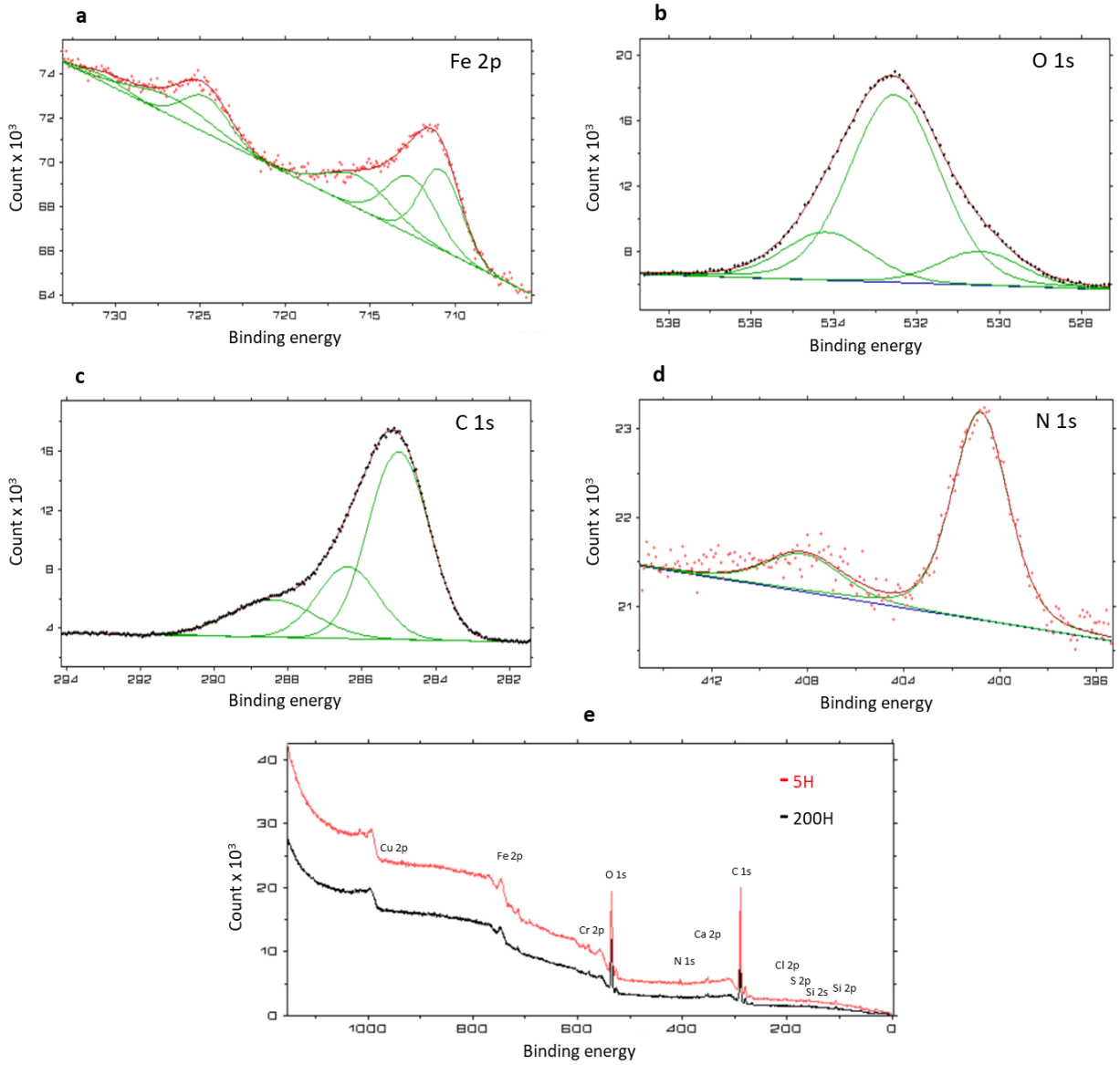

Figure 5. (Top 4 figures**)**: Fe 2p, C 1s, O 1s, N 1s XPS photoemission regions for sample 5H, obtained after iron precipitation onto the hydrochar from HTC at pH_i 0.5. (Bottom figure): Wide-range photoemission spectra for samples 5H and 200H. All the relevant species are labelled in the figure.

3.4 Arsenic adsorption

Samples obtained after Fe precipitation were tested to assess their As adsorption capacity. The comparison was carried out on the samples 5H and 200H, because the hydrochar concentration during Fe precipitation was the main parameter affecting the properties of the obtained hydrochar. The hydrochar 5H, with higher Fe_3O_4, was the only one showing a relevant As adsorption capacity

of 2.67 mg/g (± 0.01 mg/g), while no As adsorption was detected for the sample 200H. The adsorption capacity obtained for the sample 5H was higher than that obtained in a previous study with a similar two-stage HTC process (Capobianco et al., 2020), but lower than that obtained with a single alkaline stage (Capobianco et al., 2020). Notice that, a single alkaline stage was hardly applicable for water treatment, because of the remarkable adsorbent instability in water. The comparison of 5H and 200H indicated that the adsorption capacity increased by increasing the Fe/hydrochar ratio in the precipitation stage. This result suggests that Fe_3O_4 was the main group responsible for As adsorption in the composite Fe-hydrochar, as further confirmed by EDX (Fig. 6b-c). On the hydrochar surface, the adsorbed As was mainly localized close to Fe rather than to C (Fig. 6c), confirming that it was mainly adsorbed on the Fe_3O_4 functional groups. This result agrees with what was observed for magnetite-doped activated carbon fiber (Zhang et al., 2010), for which As was mainly adsorbed as monoprotonated bidentate complexes on O-containing functional groups. The O atoms involved were mainly from magnetite rather than from organic functional groups.

While the adsorbent 200H did not show any As adsorption capacity, an adsorption capacity of 1.37 mg/g was found for Fe-hydrochar composite material obtained with HTC in acid water followed by Fe^{3+} precipitation with NaOH (Fe_2O_3/$Fe(OH)_3$), despite the comparable amount of Fe on the surface (~ 6%) (Capobianco et al., 2020). This difference can be mainly attributed to the different stirring procedures adopted in the adsorption test in the two cases. In the present study, during the adsorption test, the stirring was performed using a paddle impeller, while magnetic stirring was used in the previous report. The choice of this procedure can change the extent of particle-to-particle aggregation, altering the observed adsorption capacity. To verify this effect, an adsorption test was carried with the two stirring procedures using the same adsorbent tested in the previous study (Capobianco et al., 2020). The adsorption capacity obtained with magnetic stirring was 0.8 mg/g (± 0.2 mg/g), remarkably higher ($p = 0.036$, $n = 2$) than with paddles (0.1 ± 0.2 mg/g). The difference can be due to the collision of hydrochar particles between

the magnetic bar and glass surfaces, which induces particle grinding, lower aggregation, and increased surface area. This finding underlines the need to control the parameters affecting particle interactions (such as stirring method, hydrochar concentration) during the adsorption tests for this of material. Particle-to-particle aggregation can become an important issue in fixed bed columns, the main configuration used to remove As from water.

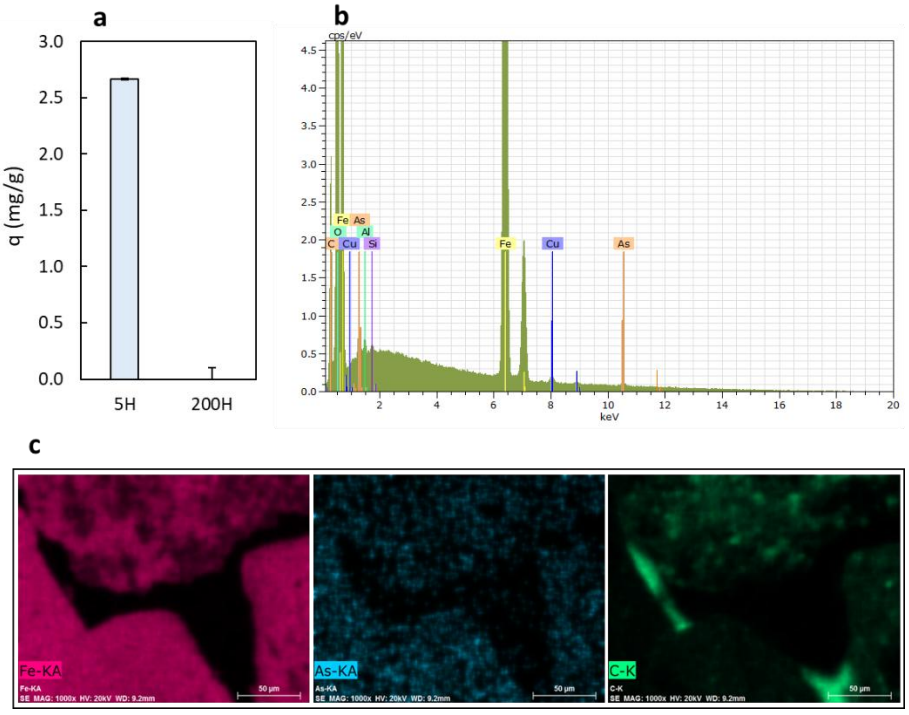

Figure 6. As adsorption capacity tests. a) As adsorption capacity measured for 5H and 200H samples, given as the average ± SD of two replicates. b) EDX spectra on 5H sample after As adsorption. c) Element mapping for Fe, As and C on the surface of the 5H sample after As adsorption.

The results of the adsorption reaction indicate that the conditions applied for preparing 5H increased substantially (~ 27 folds) the As adsorption capacity, as compared to thetwo-stage protocol previously reported (Capobianco et al., 2020). However, its application at an industrial scale, can be problematic because of the lower hydrochar concentration, requiring a higher reactor volume. A compromise for an industrial scale-up of the process could be achieved by increasing the Fe/hydrochar ratio and the hydrochar concentration. Other issues could arise in this case, such as forming of a more viscous suspension, which would require more energy for mixing.

Conclusions

The feedwater pH measured after initial biomass suspension has been shown to impact on the kinetics and yield of hydrochar synthesis. At the first stage of the process (< 30 min), the pH changes due to the release of soluble organic compounds, while eventually it changes in the opposite direction, due to the polymerization of these compounds and the production of secondary char. At lower initial pH's, the contribution of hydrolysis in the initial phase was more relevant, making the first-order kinetic model inadequate to describe the actual HTC kinetics. However, the final pH value was linearly related to the initial one and to hydrochar C% and O/C ratio.

At initial pH 0.5, the carbonization yield at 200 °C was higher than previously reported at 250 °C. This suggests that the addition of acid in the feedwater can be used to avoid a high temperature process, that would increase capital and operative costs of the HTC reactor.

In the functionalization of hydrochar with Fe_3O_4, a compromise could be conveniently chosen for the Fe/hydrochar concentration to be used. At lower hydrochar concentration, higher Fe precipitation yield and As adsorption capacity are obtained. However, this requires higher reactor volumes and produces larger Fe_3O_4 crystal structures, independent from hydrochar. A higher Fe_3O_4 fraction in the hydrochar increases the adsorption capacity for As up to 2.67 mg/g. The aggregation of hydrochar particles during the process had a great effect on the As adsorption capacity. This needs to be considered in future studies, because it can significantly affect the industrial application of this material, which is usually performed in fixed bed columns, favoring particle-to-particle aggregation.

Acknowledgments

This work was supported by the European Union in the framework of the LIFE program (BioAs project - LIFE19 ENV/IT/000512).

Reference

Astolfi, M.L., Di Filippo, P., Gentili, A., Canepari, S., 2017. Semiautomatic sequential extraction of polycyclic aromatic hydrocarbons and elemental bio-accessible fraction by accelerated solvent extraction on a single particulate matter sample. Talanta 174, 838–844. https://doi.org/10.1016/J.TALANTA.2017.06.072

ATSDR, 2019. ATSDR's Substance priority list [WWW Document]. Agency Toxic Subst. Dis. Regist. URL https://www.atsdr.cdc.gov/spl/#2019spl (accessed 4.10.20).

Azzaz, A.A., Jeguirim, M., Kinigopoulou, V., Doulgeris, C., Goddard, M.L., Jellali, S., Matei Ghimbeu, C., 2020. Olive mill wastewater: From a pollutant to green fuels, agricultural and water source and bio-fertilizer – Hydrothermal carbonization. Sci. Total Environ. 733, 139314. https://doi.org/10.1016/j.scitotenv.2020.139314

Briggs, D., Seah, M.P., 1994. Practical Surface Analysis: Auger and X-Ray Photoelectron Spectroscopy, 2nd ed. John Wiley & Son Ltd, Chichester UK.

Capobianco, L., Di Caprio, F., Altimari, P., Astolfi, M.L., Pagnanelli, F., 2020. Production of an iron-coated adsorbent for arsenic removal by hydrothermal carbonization of olive pomace: Effect of the feedwater pH. J. Environ. Manage. 273, 111164. https://doi.org/10.1016/j.jenvman.2020.111164

Chen, H., Xu, J., Lin, H., Zhao, X., Shang, J., Liu, Z., 2021. Arsenic removal via a novel hydrochar from livestock waste co-activated with thiourea and γ-Fe2O3 nanoparticles. J. Hazard. Mater. 126457. https://doi.org/10.1016/j.jhazmat.2021.126457

Di Caprio, F., Altimari, P., Uccelletti, D., Pagnanelli, F., 2014. Mechanistic modelling of copper biosorption by wild type and engineered Saccharomyces cerevisiae biomasses. Chem. Eng. J. 244, 561–568. https://doi.org/doi.org/10.1016/j.cej.2014.01.098

Driehaus, W., 2002. Arsenic removal - Experience with the GEH® process in Germany. Water Sci. Technol. Water Supply 2, 275–280. https://doi.org/10.2166/ws.2002.0073

Erses Yay, A.S., Birinci, B., Açıkalın, S., Yay, K., 2021. Hydrothermal carbonization of olive

pomace and determining the environmental impacts of post-process products. J. Clean. Prod. 128087. https://doi.org/10.1016/j.jclepro.2021.128087

Fang, J., Zhan, L., Ok, Y.S., Gao, B., 2018. Minireview of potential applications of hydrochar derived from hydrothermal carbonization of biomass. J. Ind. Eng. Chem. 57, 15–21. https://doi.org/10.1016/j.jiec.2017.08.026

Flora, J.F.R., Lu, X., Li, L., Flora, J.R.V., Berge, N.D., 2013. The effects of alkalinity and acidity of process water and hydrochar washing on the adsorption of atrazine on hydrothermally produced hydrochar. Chemosphere 93, 1989–1996. https://doi.org/10.1016/j.chemosphere.2013.07.018

Fountoulakis, M., Lahm, H.W., 1998. Hydrolysis and amino acid composition analysis of proteins. J. Chromatogr. A. https://doi.org/10.1016/S0021-9673(98)00721-3

Glibota, N., Grande Burgos, M.J., Gálvez, A., Ortega, E., 2019. Copper tolerance and antibiotic resistance in soil bacteria from olive tree agricultural fields routinely treated with copper compounds. J. Sci. Food Agric. 99, 4677–4685. https://doi.org/10.1002/jsfa.9708

Hoekman, S.K., Broch, A., Robbins, C., 2011. Hydrothermal Carbonization (HTC) of Lignocellulosic Biomass 25, 1802–1810. https://doi.org/10.1021/ef101745n

IARC, 2012. Arsenic, metals, fibres, and dusts, IARC monographs on the evaluation of carcinogenic risks to humans / World Health Organization, International Agency for Research on Cancer.

Jain, A., Balasubramanian, R., Srinivasan, M.P., 2016. Hydrothermal conversion of biomass waste to activated carbon with high porosity: A review. Chem. Eng. J. 283, 789–805. https://doi.org/10.1016/j.cej.2015.08.014

Khan, M.A., Alqadami, A.A., Otero, M., Siddiqui, M.R., Alothman, Z.A., Alsohaimi, I., Rafatullah, M., Hamedelniel, A.E., 2019. Heteroatom-doped magnetic hydrochar to remove post-transition and transition metals from water: Synthesis, characterization, and adsorption studies. Chemosphere 218, 1089–1099. https://doi.org/10.1016/J.CHEMOSPHERE.2018.11.210

Khan, N., Mohan, S., Dinesha, P., 2021. Regimes of hydrochar yield from hydrothermal degradation of various lignocellulosic biomass: A review. J. Clean. Prod. 288, 125629. https://doi.org/10.1016/j.jclepro.2020.125629

Laurent, S., Forge, D., Port, M., Roch, A., Robic, C., Vander, L., Muller, R.N., 2008. Magnetic Iron Oxide Nanoparticles: Synthesis, Stabilization, Vectorization, Physicochemical Characterizations, and Biological Applications. Chem. Rev. 108, 2064–2110. https://doi.org/10.1021/cr068445e

Li, R., Wang, J.J., Gaston, L.A., Zhou, B., Li, M., Xiao, R., Wang, Q., Zhang, Z., Huang, Hui, Liang, W., Huang, Heteng, Zhang, X., 2018. An overview of carbothermal synthesis of metal–biochar composites for the removal of oxyanion contaminants from aqueous solution. Carbon N. Y. 129, 674–687. https://doi.org/10.1016/J.CARBON.2017.12.070

Moxley, G., Zhang, Y.-H.P., 2007. More Accurate Determination of Acid-Labile Carbohydrates in Lignocellulose by Modified Quantitative Saccharification . Energy and Fuels 21, 3684–3688. https://doi.org/10.1021/ef7003893

Peydayesh, M., Mezzenga, R., 2021. Protein nanofibrils for next generation sustainable water purification. Nat. Commun. 2021 121 12, 1–17. https://doi.org/10.1038/s41467-021-23388-2

Reza, M.T., Rottler, E., Herklotz, L., Wirth, B., 2015. Hydrothermal carbonization (HTC) of wheat straw: Influence of feedwater pH prepared by acetic acid and potassium hydroxide. Bioresour. Technol. 182, 336–344. https://doi.org/10.1016/j.biortech.2015.02.024

Ungureanu, G., Santos, S., Boaventura, R., Botelho, C., 2015. Arsenic and antimony in water and wastewater: Overview of removal techniques with special reference to latest advances in adsorption. J. Environ. Manage. 151, 326–342. https://doi.org/10.1016/j.jenvman.2014.12.051

Volpe, M., Fiori, L., 2017. From olive waste to solid biofuel through hydrothermal carbonisation: The role of temperature and solid load on secondary char formation and hydrochar energy properties. J. Anal. Appl. Pyrolysis 124, 63–72. https://doi.org/10.1016/j.jaap.2017.02.022

Wang, Tengfei, Zhai, Y., Zhu, Y., Peng, C., Xu, B., Wang, Tao, Li, C., Zeng, G., 2017. Acetic Acid

and Sodium Hydroxide-Aided Hydrothermal Carbonization of Woody Biomass for Enhanced Pelletization and Fuel Properties. Energy and Fuels 18, 12200–12208. https://doi.org/10.1021/acs.energyfuels.7b01881

Zhang, S., Li, X. yan, Chen, J.P., 2010. An XPS study for mechanisms of arsenate adsorption onto a magnetite-doped activated carbon fiber. J. Colloid Interface Sci. 343, 232–238. https://doi.org/10.1016/J.JCIS.2009.11.001

Zhu, X., Liu, Y., Zhou, C., Zhang, S., Chen, J., 2014. Novel and high-performance magnetic carbon composite prepared from waste hydrochar for dye removal. ACS Sustain. Chem. Eng. 2, 969–977. https://doi.org/10.1021/sc400547y

Zoroufchi Benis, K., Motalebi Damuchali, A., McPhedran, K.N., Soltan, J., 2020. Treatment of aqueous arsenic – A review of biosorbent preparation methods. J. Environ. Manage. 273, 111126. https://doi.org/10.1016/J.JENVMAN.2020.111126